CHINESE OPTICS LETTERS

Vol. 24, No. 6 | June 2026

Deep-learning-assisted microprism waveguide design toward enhanced optical performance in AR displays

Bo Wang (王 博), Lingbao Kong (孔令豹)*, Huixin Song (宋慧鑫), Xinlan Tang (唐鑫岚), Zhenzhen Ding (丁臻帧), and Junhua Wang (王军华)

Shanghai Engineering Research Center of Ultra-precision Optical Manufacturing, College of Future Information Technology, Fudan University, Shanghai 200438, China

*Corresponding author: lkong@fudan.edu.cn

Received October 13, 2025 | Accepted January 27, 2026 | Posted Online June 11, 2026

Commercial augmented reality (AR) glasses commonly employ geometrical or diffractive optical waveguides, which, despite their compact form factor, typically suffer from low optical efficiency. To achieve both thin form and high efficiency, for the first time, an AR optical waveguide based on a microprism is proposed. A deep-learning-assisted hardware–software co-optimization framework is introduced to expand the system's design freedom and enable end-to-end joint optimization between the microprism waveguide and the image preprocessing algorithm. Simulation results demonstrate that the proposed system achieves an overall thickness of only 8 mm, an optical efficiency of approximately 44.3%, high imaging quality, and a binocular field of view of 36°. This work provides a new pathway toward high-performance and ultra-thin AR display systems.

Keywords: microprism; augmented reality; optical waveguide; deep learning optimization; hardware–software co-design.

© The Authors. Published by Chinese Laser Press under a Creative Commons Attribution 4.0 International License. Distribution or reproduction of this work in whole or in part requires full attribution of the original publication, including its DOI.

DOI: 10.3788/COL202624.062201

1. Introduction

Augmented reality (AR) is evolving into a next-generation computing platform, yet its optical systems often face inherent trade-offs among device thickness, optical efficiency, and imaging performance. Current commercial AR glasses primarily employ geometrical or diffractive optical waveguides, which offer compact form factors but typically suffer from low optical efficiency. A decrease in optical efficiency leads directly to elevated power consumption, thereby shortening operational battery life—one of the principal impediments to the large-scale adoption of current AR glasses. Ergonomic considerations demand lightweight and compact designs to enhance user comfort and portability, thereby imposing stringent challenges on optical design, including trade-offs in performance, dynamic range, and vergence–accommodation conflict (VAC)[1].

Existing AR optical architectures mainly include reflective, diffractive, and geometrical waveguides. Reflective optical systems can achieve high image quality and wide field of view (FOV) but at the expense of increased structural complexity and system thickness, often exceeding 16 mm[2,3]. Cheng *et al.* designed a freeform prism-based head-mounted display that maintains high image quality and wide FOV with an optical thickness below 9.5 mm[4,5]. Diffractive waveguides can further reduce system thickness to around 1.5 mm; however, their optical efficiency typically falls below 10%, and they operate within a narrow spectral bandwidth[6,7]. Geometrical waveguides exhibit compactness with a thickness of approximately 2.3 mm and an optical efficiency of about 20%, yet their imaging uniformity is highly sensitive to mirror alignment, multilayer coating quality, and manufacturing tolerances[1,8–10]. In addition, metasurface-based approaches still encounter challenges in terms of efficiency, fabrication cost, and broadband optimization[11–15]. Overall, conventional optical designs are constrained by the coupled trade-offs among thickness, optical efficiency, and imaging performance, which make further optimization increasingly difficult.

To address these limitations, we propose a novel AR optical waveguide based on a microprism that achieves simultaneous thinness, high optical efficiency, and superior imaging quality. The microprism can be efficiently fabricated through single-point diamond turning and injection molding. During light propagation, the proposed waveguide ensures total internal reflection (TIR) for efficient light transmission, while a semi-transparent beam-splitting coating enables the simultaneous delivery of virtual and real-world images to the human eye.

Unlike previous optical–algorithm co-design studies that primarily focus on post-capture image processing[16,17], our method emphasizes pre-projection image preprocessing to alleviate the optical design burden and preemptively correct chromatic aberration and geometric distortion. End-to-end joint optimization between optical components and computational algorithms has been successfully applied in various fields, including extended depth of field[16,18–21], super-resolution imaging[22], aberration correction[23], and high dynamic range imaging[24]. Building on the differentiable ray-tracing framework[23], we adapt the code to AR display design by integrating a microprism waveguide model, thereby enabling a deep-learning-assisted hardware–software co-optimization platform.

Simulation results demonstrate that the proposed microprism waveguide achieves a total system thickness of only 8 mm, an optical efficiency of approximately 44.3%, a binocular FOV of 36°, and high-quality imaging performance. This approach provides a new pathway toward lightweight, energy-efficient, and high-performance AR display systems.

2. Method

As illustrated in Fig. 1(a), the microprism waveguide AR display consists of two optical paths: one dedicated to virtual image projection and the other for direct observation of real-world scenes. Figure 1(b) presents the structural composition of the system, which integrates two microprism surfaces—surface 1 and surface 4—alongside an anamorphic aspheric surface (surface 2) (Supplementary Material, Sec. S2).

The microprism closer to the eye facilitates the formation of virtual images, while the microprism positioned farther from the eye serves as an auxiliary element, preserving an undistorted see-through view of the external environment. As illustrated in Fig. 1(a), light emitted from a specific point on the display first undergoes refraction at surface 3, adjacent to the display, then sequentially reflects off surfaces 2′, 1′, and 2, and finally transmits through surface 1 to reach the exit pupil of the system. The base surface 2′ of the microprism lens and the microprism surface 1′ must satisfy the condition for TIR. Surface 2 of the prism is coated with a semi-reflective layer to enable optical see-through functionality. Light originating from the display is reflected by surface 2, while light from the real-world scene is transmitted through. The microprism waveguide AR display consists of two bonded lenses, with their bonding surfaces joined using Norland 136 adhesive. As illustrated in Fig. 1(c), the sag of the original surface is described by Eq. (1),

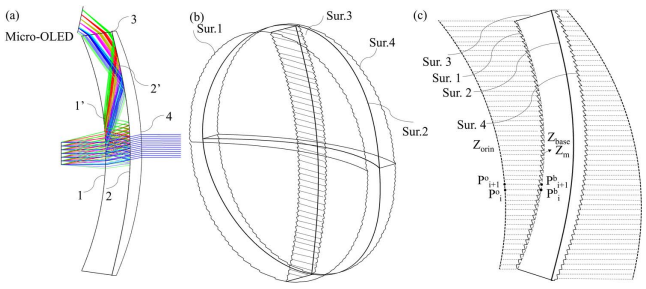

Fig. 1. Overall structure and optical path of the designed microprism waveguide system. (a) Optical path schematic of the microprism waveguide, illustrating the light propagation from the micro-OLED display. (b) Structural representation of the designed microprism waveguide, showing key surfaces (surfaces 1–4). (c) Detailed schematic of the microprism surface design, including layer profiles and structural parameters.

$$Z_{\text{orin}}(x,y)=\frac{c_o r^2}{1+\sqrt{1-(1+k_o)c_o^2 r^2}}+\sum_{n=1}^{N}\alpha_n r^{2n}+\sum_{l}^{L}\gamma_l Z_l\left(\frac{x}{R},\frac{y}{R}\right). \tag{1}$$

Here, c_o denotes the curvature of the original surface, and k_o is the conic constant. $r=\sqrt{x^2+y^2}$ represent the radial coordinate. The coefficients α_n correspond to the even-order aspheric terms of the original surface, and $Z(x/R,y/R)$ denotes the Zernike polynomial used to describe higher-order surface deviations, with γ_l representing the corresponding Zernike coefficients. The sag of the base surface can, thus, be expressed as

$$Z_{\text{base}}(x,y)=\frac{c_b r^2}{1+\sqrt{1-(1+k_b)c_b^2 r^2}}+\sum_{m=1}^{M}\alpha_m r^{2m}. \tag{2}$$

Here, c_b denotes the curvature of the base surface, k_b is the conic constant, and α_m represents the even-order aspheric coefficients of the original surface. We define

$$\xi(x,y)\doteq Z_{\text{orin}}(x,y)-Z_{\text{base}}(x,y). \tag{3}$$

If the distance between P_{i+1}^o and P_i^o is T, then the sag of the microprism surface can be expressed as

$$Z_m^i(x,y)=Z_{\text{base}}(x,y)+\xi(x,y)-\xi[(i-1)T],\quad (x,y)\in\Omega_i. \tag{4}$$

Here, Ω_i denotes the spatial domain corresponding to the ith microprism. Z_m^i represents the sag of the ith microprism surface, P_i^o and P_i^b denote the sag of the thinned surface Z_{orin} and Z_{base}, respectively, along the spherical meridional direction corresponding to the ith periodic length. T denotes the period of the microprism. The use of Eq. (4) characterizes the microprism with specific features. By substituting Eqs. (1)–(4), it can be shown that the surface normals of the microprism surface are consistent with those of the original surface, i.e.,

$$\frac{\partial Z_m^i(x,y)}{\partial x}=\frac{\partial Z_{\text{orin}}(x,y)}{\partial x},\quad \frac{\partial Z_m^i(x,y)}{\partial y}=\frac{\partial Z_{\text{orin}}(x,y)}{\partial y}. \tag{5}$$

According to Snell's law and Eq. (5), the microprism surface produces the same deflection effect on the incident rays as the original surface.

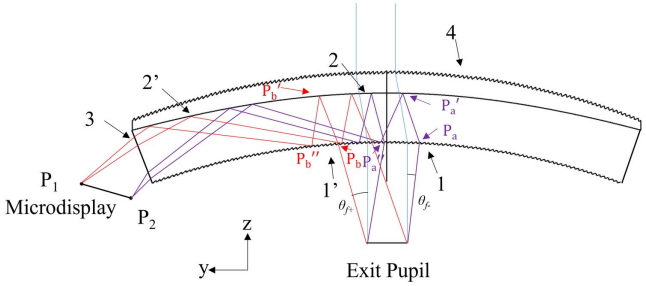

Fig. 2. Optical path of rays of different object fields and different pupil positions in the microprism waveguide: the incident angles of the rays on surfaces 2′ and 1′ depend on their field and pupil positions, and they are controlled to satisfy TIR conditions.

Equation (4) enables the transformation of a thick lens into a thinned structure conforming to the base surface, with a thinning ratio of D/d, where D denotes the lens aperture and d is the final thickness. Fresnel lenses adopt a concentric ring-shaped microprism for focusing or collimation, while our microprism is linearly arranged to enable directional light control, better suited to AR applications. Unlike dispersion-sensitive and complex-to-manufacture metasurfaces, microprism surfaces operate across a broad spectral range, exhibit high optical transmittance, and feature microprism with thicknesses on the order of tens of microns, making them well-suited for most thinning applications. Using Eq. (4), the microprism surface can be represented with fewer parameters, facilitating a more efficient optimization process.

Throughout the optimization process, the unit direction vector of the light ray $\mathbf{k}_1$ and the surface normal vector $\hat{\mathbf{u}}$ must satisfy the constraints of the TIR, as shown in Fig. 2. Here, $n_{1,2}$ represent the refractive indices of the media on the incident and emergent sides of the light ray, respectively. K26R is used as the injection molding material for the lenses, and the two lens bonding surfaces are bonded. The light emitted from the display first enters the waveguide, undergoes TIR at the bonded interface, and then experiences another TIR at the waveguide–air interface. Using Eq. (6), the conditions for valid light rays are determined, ensuring that only light undergoing TIR can be transmitted from the display to the human eye,

$$\left(\frac{n_1}{n_2}\right)^2 [1 - (\mathbf{k}_1 \cdot \hat{\mathbf{u}})^2] > 1. \tag{6}$$

On the double bonding surface, a semi-transparent and semi-reflective coating is required for the region, where $P_a' < y < P_b'$. TIR plays a crucial role in constraining the FOV of the AR display, with θ_{f-} being limited by TIR angle of region 1′ $(P_a < y < P_b)$ and θ_{f+} being constrained by the TIR of region 2′. The TIR angle is further influenced by the injection molding material and the bonding materials utilized in the fabrication process. With the intentional 50:50 power split introduced by the semi-reflective coating and the Fresnel losses at the microprism-related interfaces taken into account, the resulting optical efficiency is approximately 44.3%; applying anti-reflection coatings on the relevant interfaces would further suppress Fresnel reflections and increase the efficiency toward the film-limited upper bound of approximately 50% for the current splitting design. Further details, including the surface-resolved efficiency breakdown and related analysis, are given in the Supplementary Material, Sec. S8.

In pursuit of an ultralightweight design, the number of optical surfaces is significantly minimized, thereby restricting the available optimization space. To mitigate the burden of optical design, we introduce a deep-learning-based framework[25] for AR display design. The end-to-end AR display design framework integrates a deep-learning-trained neural network to preprocess images from the display, effectively reducing distortions and aberrations. This framework employs an end-to-end optimization strategy, ensuring seamless synergy between algorithmic processing and optical design, ultimately yielding an optimized microprism-based AR display system.

The end-to-end AR display design framework is based on a differentiable ray-tracing framework[25], as illustrated in Fig. 3. During the forward image simulation process, deep neural network θ' first performs image preprocessing, after which the preprocessed image is displayed on the OLED screen and subsequently propagates through the microprism waveguide before reaching the human eye. The employed image preprocessing network and the joint optimization strategy are detailed in the Supplementary Material, Sec. S6. Throughout this process, the gradients of each optical parameter θ (including surface curvature, position, conic coefficients, microprism's parameters, and polynomial coefficients) are tracked. In the backpropagation

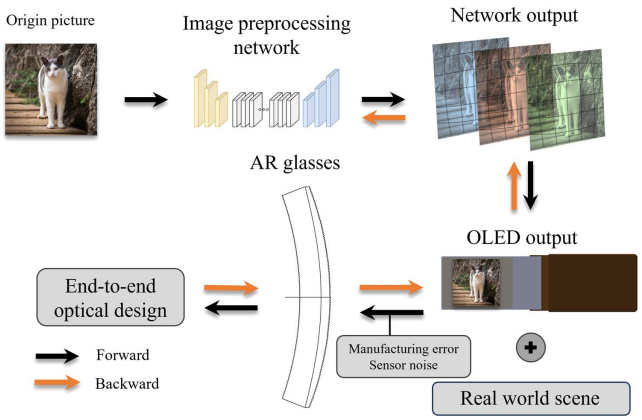

Fig. 3. End-to-end AR display design framework. A differentiable ray-tracing framework is employed to simulate the monocular eye-captured image from a given origin image. The origin image is first processed by an image preprocessing neural network and then transmitted through the microprism-based waveguide AR glasses to the human eye. During the forward simulation process (indicated by black arrows), the gradients of each optical parameter are tracked. The errors are subsequently backpropagated (orange arrows) from both the simulated image and the final network output, thereby enabling end-to-end joint optimization that integrates optical system design and image reconstruction.

phase, the error between the target image and the perceived image is propagated backward to optimize both the microprism waveguide and the image preprocessing network,

$$\theta, \theta' = \arg \min \|\tilde{I}(I;\theta,\theta') - I\|_2^2. \tag{7}$$

The input image I is first processed through a deep learning network $F(I;\theta')$, which maps the undistorted image across different color channels to a distortion- and aberration-compensated image. The training dataset used is DIV2K. Generalization analysis on the validation set is provided in the Supplementary Material, Sec. S7, and the training curve and convergence behavior are presented in the Supplementary Material, Sec. S6. The preprocessed image is then propagated through the microprism waveguide, where it undergoes convolution with the point spread function (PSF) p_λ of the microprism waveguide and is ultimately projected to the human eye,

$$I_c(x,y) = \int \{\tilde{I}[F(I;\theta') * h_{\mathrm{OLED}}] * p_\lambda\}(x,y)\kappa_c(\lambda)\mathrm{d}\lambda. \tag{8}$$

Here, κ_c denotes the human eye's sensitivity function to different wavelengths, h_{OLED} represents the influence of the OLED display on the system, and the symbol $*$ represents convolution. The detailed derivation of the point spread function for the microprism surface is provided in the Supplementary Material, Sec. S1. The influence of the microprism on the optical system is analogous to the effect of multiple convolutional kernels in a deep learning network, where each microprism modulates the local light field in a manner similar to spatially varying convolutional filters. Consistent with the ray-based image-formation model described above, the pre-compensation network is designed to correct display-domain errors that can be expressed as a two-dimensional spatial remapping, including geometric distortion and lateral chromatic shift. It does not physically modify the optics and, therefore, does not provide true correction of higher-order aberrations that manifest as field-dependent PSF blur, which would require explicit wave-optics or field-dependent PSF modeling together with additional wavefront-control degrees of freedom.

3. Result

As shown in Fig. 4, the use of a neural network for pre-compensation of chromatic aberration and geometric distortion proves to be highly effective. Figure 4(a) shows the original image, in which the background railing appears straight. However, after passing through the designed microprism-based AR display, noticeable distortion and chromatic aberration are observed—most notably, lateral chromatic aberration appears along the edges of the cat's foot [Fig. 4(b)]. Although the visual effects in Fig. 4 are slightly limited due to size constraints, the corresponding enlarged images provided in the Supplementary Material, Fig. S4, more clearly reveal the chromatic fringing and geometric distortion. The resulting image yields a peak signal-to-noise ratio (PSNR) of 11.86 dB and a structural similarity index measure (SSIM) of 0.5471, indicating significant degradation.

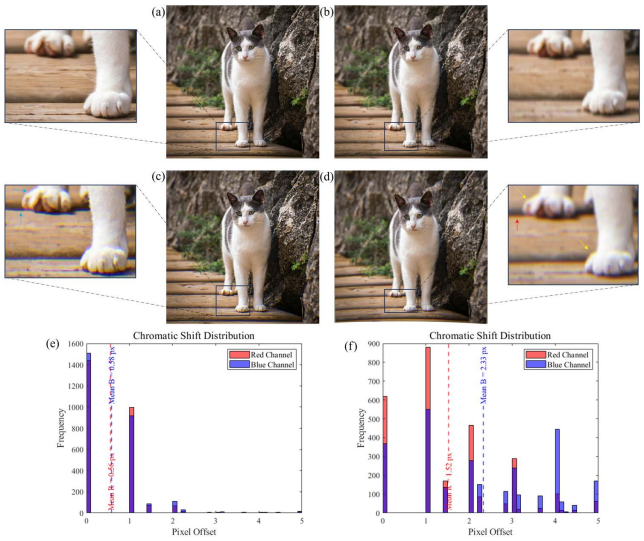

Fig. 4. Comparison of image distortion and chromatic aberration correction induced by the microprism. (a) Ground truth image. (b) Simulation-based final display result after end-to-end compensation. (c) Output of the image preprocessing network. (d) Image directly rendered without any preprocessing. (e) Chromatic shift distribution corresponding to the black box region in (b). (f) Chromatic shift distribution corresponding to the black box region in (c).

When the original image is pre-compensated by a neural network to correct for both geometric distortion and chromatic aberration, the resulting image—after passing through the same microprism-based AR display—shows substantial improvement. As illustrated in Fig. 4(c), both types of aberrations are effectively mitigated, demonstrating the effectiveness of the pre-compensation strategy. The improvement is also more visually evident in the Supplementary Material, Fig. S4. The PSNR and SSIM of the corrected image reach 19.62 dB and 0.8438, respectively. Figure 5 presents the virtual image displayed through the microprism waveguide after joint optimization [Fig. 5(a)], as well as the MTF of the real-world scene observed through the microprism waveguide and compensating lens [Fig. 5(b)]. The MTF was evaluated at a pupil diameter of 4 mm, across representative field angles including the optical axis and edge of the FOV.

In the Supplementary Material, we present the imaging performance of a fabricated microprism surface when applied to real-world scenes. A laser-based demonstration was conducted to visualize the light propagation within the microprism waveguide (Supplementary Material, Sec. S3).

To assess potential stray-light and ghost-image artifacts in the proposed microprism-based AR waveguide, we conducted non-sequential ray tracing over the sampled field angles and monitored the irradiance distribution on a detector placed at the eyebox plane (Supplementary Material, Fig. S9). The simulation shows that a fraction of rays is transmitted through the semi-reflective film and continues propagating inside the waveguide, while another fraction undergoes additional reflections at the

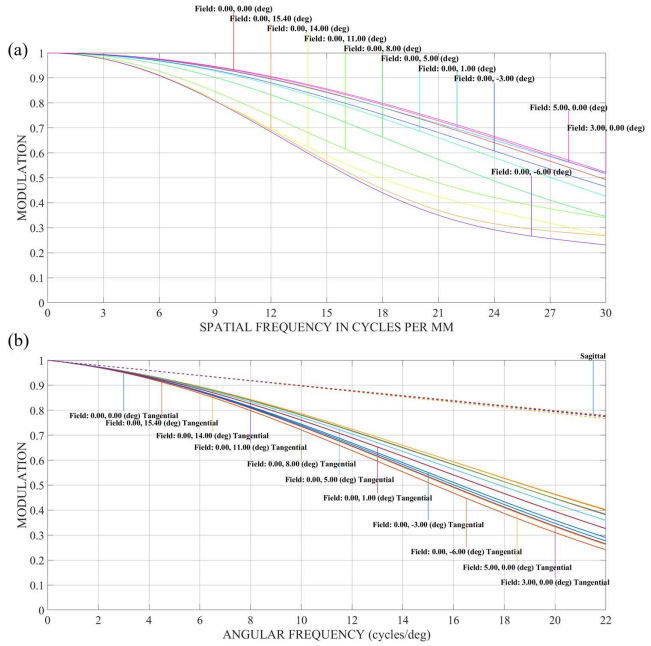

Fig. 5. The initial structure of the microprism-based AR display concerning MTF for (a) virtual image display and (b) real-world scene observation.

microprism interfaces and forms secondary exit paths. Importantly, the resulting stray-light spot is spatially separated from the primary coupling-out region, and the corresponding secondary exit is located 20.3 mm away from the eyebox center, indicating a low likelihood of overlap with the viewing zone and, thus, a low probability of forming a visible ghost image. A residual ghost contribution could only occur if the transmitted component is reflected toward the eye by the compensation optics and re-enters the nominal eyebox; this return path is inherently weak and can be further suppressed by applying an AR coating on the rear surface of the compensation lens. Further mitigation strategies include AR coatings on microprism surfaces and locally reducing the microprism fill factor in selected regions to interrupt residual-ray propagation.

We also assessed the see-through distortion of the proposed waveguide and found only minor geometric distortion across the designed FOV, with the corresponding distortion grid provided in the Supplementary Material, Fig. S5.

Table 1. Performance of the System.

Parameter	Value
FOV (binocular)	36°
Eye box ($H \times V$)	8 mm × 6 mm
MTF of virtual imaging	>0.23 at 30 lp/mm
Wavelength	656.3–486.1 nm
Optical efficiency	≈44.3%
System thickness	8 mm

4. Conclusion

In this work, we proposed and demonstrated a novel AR optical waveguide based on a microprism. By combining geometric optics with deep-learning-assisted optimization, the proposed system achieves a compact optical configuration that simultaneously ensures high efficiency and imaging quality. The microprism enables TIR-based light guiding with minimal thickness, while a semi-transparent beam-splitting coating allows the seamless integration of virtual and real-world imagery. Furthermore, a differentiable ray-tracing framework was incorporated to enable end-to-end joint optimization between the optical design and the image preprocessing network. This synergistic approach effectively compensates for geometric distortion and chromatic aberration, significantly enhancing visual fidelity. Simulation results confirm that the optimized system achieves a total thickness of only 8 mm, an optical efficiency of approximately 44.3%, and a binocular FOV of 36°, while maintaining high image quality and see-through performance, as summarized in Table 1. Overall, this work establishes a promising design paradigm for next-generation AR display systems by bridging optical engineering and computational optimization. The proposed microprism-based waveguide provides a lightweight, energy-efficient, and scalable solution for compact AR devices, paving the way for future integration of optical–computational co-design in wearable display technologies.

Acknowledgements

This work was supported by the National Natural Science Foundation of China (No. 52375414) and the Science and Technology Commission of Shanghai Municipality (Nos. 23ZR1404200 and 24511106602).

References

1. D. Cheng, Q. Wang, Y. Liu, *et al.*, "Design and manufacture AR head-mounted displays: a review and outlook," Light Adv. Manuf. **2**, 24 (2021).
2. H. Hua, Y. Ha, and J. P. Rolland, "Design of an ultralight and compact projection lens," Appl. Optics **42**, 97 (2003).
3. Z. Zheng, X. Liu, H. Li, *et al.*, "Design and fabrication of an off-axis see-through head-mounted display with an *x*–*y* polynomial surface," Appl. Optics **49**, 3661 (2010).
4. D. Cheng, H. Chen, C. Yao, *et al.*, "Design, stray light analysis, and fabrication of a compact head-mounted display using freeform prisms," Optics Express **30**, 36931 (2022).
5. D. Cheng, Y. Wang, H. Hua, *et al.*, "Design of an optical see-through head-mounted display with a low *f*-number and large field of view using a freeform prism," Appl. Optics **48**, 2655 (2009).
6. P. Äyräs, P. Saarikko, and T. Levola, "Exit pupil expander with a large field of view based on diffractive optics," J. Soc. Inform. Disp. **17**, 659 (2009).
7. M. G. Moharam, D. A. Pommet, E. B. Grann, *et al.*, "Stable implementation of the rigorous coupled-wave analysis for surface-relief gratings: enhanced transmittance matrix approach," J. Optical Soc. Am. A **12**, 1077 (1995).

8. J. W. Pan and H. C. Hung, "Optical design of a compact see-through head-mounted display with light guide plate," J. Disp. Technol. **11**, 223 (2015).
9. J. Yang, P. Twardowski, P. Gérard, *et al.*, "Design of a large field-of-view see-through near to eye display with two geometrical waveguides," Optics Lett. **41**, 5426 (2016).
10. K.-W. Zhao and J.-W. Pan, "Optical design for a see-through head-mounted display with high visibility," Optics Express **24**, 4749 (2016).
11. M. Gopakumar, G.-Y. Lee, S. Choi, *et al.*, "Full-colour 3D holographic augmented-reality displays with metasurface waveguides," Nature **629**, 791 (2024).
12. G.-Y. Lee, J.-Y. Hong, S. Hwang, *et al.*, "Metasurface eyepiece for augmented reality," Nat. Commun. **9**, 4562 (2018).
13. Y. Li, S. Chen, H. Liang, *et al.*, "Ultracompact multifunctional metalens visor for augmented reality displays," PhotoniX **3**, 29 (2022).
14. X. He, Z. Zhang, D. Ma, *et al.*, "Erbium-doped/erbium-ytterbium co-doped waveguide amplifiers in silicon-based optoelectronics: recent progress," Adv. Photonics **7**, 064001 (2025).
15. K. Sun, Y. Cai, Y. Kivshar, *et al.*, "Flatband high-*Q* metasurfaces inspired by coupled-resonator optical waveguides," Adv. Photonics **7**, 056008 (2025).
16. V. Sitzmann, S. Diamond, Y. Peng, *et al.*, "End-to-end optimization of optics and image processing for achromatic extended depth of field and super-resolution imaging," ACM Trans. Graph. **37**, 114 (2018).
17. G. Wetzstein, A. Ozcan, S. Gigan, *et al.*, "Inference in artificial intelligence with deep optics and photonics," Nature **588**, 39 (2020).
18. Z. Niu, J. Wang, Y. Tian, *et al.*, "Wavefront-coded phase measuring deflectometry for the all-focused measurement," Optics Lett. **47**, 4770 (2022).
19. S. Pinilla, S. R. Miri Rostami, I. Shevkunov, *et al.*, "Hybrid diffractive optics design via hardware-in-the-loop methodology for achromatic extended-depth-of-field imaging," Optics Express **30**, 32633 (2022).
20. Q. Sun, C. Wang, Q. Fu, *et al.*, "End-to-end complex lens design with differentiate ray tracing," ACM Trans. Graph. **40**, 71 (2021).
21. X. Yang, M. Souza, K. Wang, *et al.*, "End-to-end hybrid refractive-diffractive lens design with differentiable ray-wave model," in *SIGGRAPH Asia 2024 Conference Papers* (2024), p. 47.
22. Q. Sun, J. Zhang, X. Dun, *et al.*, "End-to-end learned, optically coded super-resolution SPAD camera," ACM Trans. Graph. **39**, 9 (2020).
23. J. Zhou, S. Chen, Z. Ren, *et al.*, "Revealing the preference for correcting separated aberrations in joint optic-image design," Opt. Lasers Eng. **178**, 108220 (2024).
24. Q. Sun, E. Tseng, Q. Fu, *et al.*, "Learning rank-1 diffractive optics for single-shot high dynamic range imaging," in *2020 IEEE/CVF Conference on Computer Vision and Pattern Recognition (CVPR)* (2020) p. 1383.
25. X. Yang, Q. Fu, and W. Heidrich, "Curriculum learning for ab initio deep learned refractive optics," Nat. Commun. **15**, 6572 (2024).